

Fluorescence Microscopic Investigations of Molecular Dynamics in Self-Assembled Nanostructures

Takashi Ito* and Daniel A. Higgins*

* To whom correspondence should be addressed.

Prof. T. Ito and Prof. D. A. Higgins

Department of Chemistry, Kansas State University, 213 CBC Building, Manhattan, KS 66506-0401, USA

Emails: ito@ksu.edu (TI), higgins@ksu.edu (DAH)

Telephone: 785-532-1451 (TI), 785-532-6371 (DAH)

Fax: 785-532-6666 (TI and DAH)

ORCID: 0000-0001-7443-3157 (TI), 0000-0002-8011-2648 (DAH)

Abstract

Many analytical methods employ self-assembled nanostructured materials as chemical recognition media. Molecular permeation through these materials exhibits unique selectivity owing to nanoconfinement-induced enhancement of permeant–nanostructure interactions. This Personal Account introduces our efforts to investigate the detailed dynamics of single or a small number of molecules in nanostructured materials. We developed new experimental and analysis approaches built upon laser-based fluorescence microscopy to measure the detailed translational and orientational dynamics of molecules diffusing in horizontally-oriented, cylindrical nanostructures, including surfactant micelles, silica mesopores, block copolymer microdomains, and bolaamphiphile-based organic nanotubes. Our studies clarified nanoscale details on the structural/chemical heterogeneity of the nanostructures, and their impacts on molecular mass transport dynamics.

Keywords: single-molecule studies • fluorescence spectroscopy • self-assembly • nanostructures • noncovalent interactions

1. Introduction

Self-assembled nanostructures based on synthetic molecules and macromolecules have been explored for myriad applications. These nanostructures are constructed from molecular building blocks by simple solution-based processes without the use of sophisticated instruments. More importantly, their morphologies, dimensions, and chemical properties can be tuned through the rational design of their constituents. In analytical sciences, self-assembled nanostructures are utilized to enhance the efficiency of chemical separations and detection. For example, surfactant micelles have been added to a mobile phase in capillary electrophoresis for separations of neutral analytes in a method known as micellar electrokinetic chromatography.^[1] Monolithic nanoporous materials have served as chromatographic stationary phases for highly-selective, high-speed separations.^[2] Free-standing nanoporous polymer and ceramic membranes have been widely used for water desalination and purification.^[3,4] Thin films incorporating self-organized nanostructures permit the control of the selectivity and sensitivity of electrochemical sensors.^[5,6] Nanoporous materials based on metal-ligand coordination networks have been explored for highly-selective chemical separations and analysis.^[7-11] Selectivity in these analytical methods is basically controlled by the partitioning, sorption, and permeation of target species in the chemically heterogeneous nanostructures that are regulated by steric, electrostatic, and chemical interactions between the permeants and nanostructures.^[12] Thorough knowledge about the effects of nanoscale environments on these dynamic processes will help design nanostructures suitable not only for these analytical applications but also for other applications such as chemical reactions and energy storage.^[13-15]

Molecular dynamic behaviors in self-assembled nanostructures are usually assessed using ensemble-averaged methods that measure the behavior of a large number of molecules located

under different local environments. Conventionally, molecular transport mechanisms in nanostructured materials are investigated by systematically measuring flux data of different solutes across their monolithic membranes under different conditions.^[16,17] Unfortunately, flux data cannot directly provide information on molecular-level dynamics owing to their ensemble-averaged nature. In addition, their interpretation is often complicated by other factors that control solute flux, including solute partitioning from a feed solution into the membranes,^[18,19] and the structural properties of the membranes such as porosity, tortuosity, and defects.^[17] A number of methods based on NMR^[20,21] and quasi-elastic neutron scattering^[22] have been used to elucidate distinct molecular-level mechanisms inside nanostructured materials. However, these spectroscopic measurements cannot afford the detailed distribution of spatiotemporal molecular behaviors associated with local materials heterogeneity owing to their extensive ensemble averaging, as with flux measurements.

Microscopic methods have been employed to measure the local morphologies, sizes, and chemical properties of nanostructured materials. In particular, fluorescence microscopic techniques enable *in situ* monitoring of solute dynamics in nanostructured materials under ambient conditions.^[12,23,24] For example, fluorescence recovery after photobleaching (FRAP)^[25,26] has been used to measure ensemble-averaged molecular diffusion in micron-scale regions of nanostructured materials. Fluorescence correlation spectroscopy (FCS)^[26] and imaging FCS^[27] give quantitative information on the dynamics of a small number of molecules passing through a femtoliter detection volume in nanostructured materials. Furthermore, single-molecule tracking (SMT) allows for monitoring the positions of individual probe molecules with the precision of tens of nanometers, well below the diffraction-limited spatial resolution of conventional far-field optics.^[28,29] The trajectory of the motion of a single molecule, which is obtained by linking its positions in

successive video frames, gives rich information on the spatiotemporal dynamics of the molecule, such as permeation and adsorption/desorption.^[23,30,31] A trajectory also gives insights into the morphological and chemical properties of a nanostructure that serves as the molecular pathway.^[23,30-33]

Herein, we introduce our approaches to unveiling the detailed dynamics of fluorescent solute molecules in self-assembled nanostructured materials, including surfactant-filled silica mesopores (**Figure 1a**), cylindrical block copolymer (BCP) microdomains (**Figure 1b**), and bolaamphiphile-based organic nanotubes (ONTs) (**Figure 1c**), using advanced fluorescence methods built on SMT and FCS.^[12,34,35] We have established a number of measurement and analysis methods including (1) orthogonal regression methods (ORM) for the quantitative analysis of 1D trajectories^[36,37] and nanostructure characterization;^[38-44] (2) FRAP-SMT for direct comparison of ensemble and single-molecule diffusion behavior;^[45] (3) SMT with simultaneous single-molecule emission polarization measurements (SMT-SMEP) for quantitative measurements of translational and orientational molecular dynamics;^[46-48] and (4) two-color SMT for simultaneous measurements of the distribution and diffusion of single solvatochromic molecules.^[48] We also employed imaging FCS for assessing molecular diffusion in individual ONTs.^[35,49-51] These methods have elucidated the structural and chemical properties of nanostructures, and also have provided invaluable insights into the detailed molecular diffusion dynamics in the nanostructures.

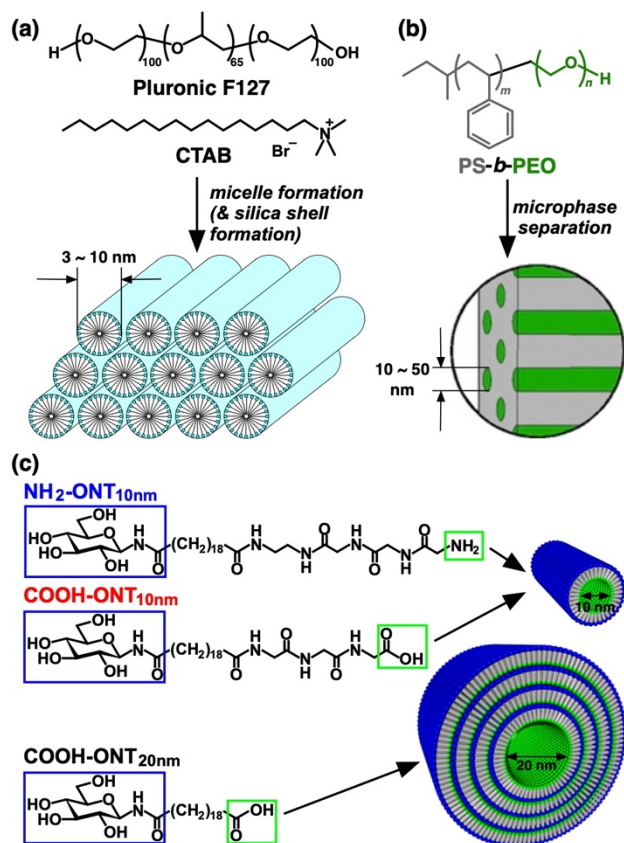


Figure 1. Materials incorporating self-assembled cylindrical nanostructures used in our studies. Adapted with permission from Ref. 35. Copyright 2020 American Chemical Society.

2. Experimental Considerations and Data Analysis

2.1. Self-Assembled Cylindrical Nanostructures

Many membrane materials used for real chemical separations comprise nanostructures that are heterogeneous in their sizes, shapes, and chemical compositions. The heterogeneous nature of these materials impedes the fundamental investigation of detailed molecular transport processes. In addition, these membranes are often opaque, preventing sensitive fluorescence measurements owing to high background signals caused by light scattering.

We have employed materials incorporating self-organized cylindrical nanostructures of uniform diameters ranging from 3-50 nm (**Figure 1**). The symmetric cylindrical structures simplify data interpretation associated with solute-nanopore interactions. Thin films of these materials are

colorless and transparent, permitting us to measure fluorescence emission from single molecules. Most importantly, molecular motions along these horizontally-oriented, cylindrical nanostructures are observed as one-dimensional (1D) trajectories in SMT data, which facilitates quantitative data analysis using the ORM as discussed below.

Specifically, we have investigated solute diffusion along flow-aligned rod-shaped surfactant micelles and silica mesopores in microchannels (**Figure 1a**),^[38,40,42,52] surfactant-templated silica mesopores in substrate-supported thin films (**Figure 1a**),^[36,44,46-48] cylindrical microdomains in thin polystyrene-*block*-poly(ethylene oxide) (PS-*b*-PEO) films (**Figure 1b**),^[39,41,43,45] and substrate-immobilized ONTs (**Figure 1c**).^[35,49-51] Rod-shaped micelles with diameters of 3–10 nm can be obtained by adjusting material compositions to give a hexagonal mesophase.^[38,53] Cylindrical PEO microdomains (10 – 50 nm in diameter) are formed from PS-*b*-PEO having appropriate PEO volume fractions (*i.e.*, 0.2 – 0.3).^[54,55] ONTs having uniform inner diameters (10 or 20 nm) with controlled inner (-NH₂ or -COOH) and outer glucose groups are self-assembled from rationally designed bolaamphiphiles.^[56] The walls of the resulting single-wall and quadruple-walled ONTs consist of hydrocarbon chains with and without oligoglycine-based hydrogen bonding networks, respectively.

2.2. Fluorescent Solute Molecules

Rhodamine (**Figure 2a**)^[35,49,51] and perylene diimide (PDI) (**Figure 2b**) dyes having different net charges and hydrophobicity have been used to investigate the effects of steric, electrostatic, and hydrophobic interactions on their diffusion dynamics. Among them, SRB has permitted us to investigate the morphology and permeability of PEO microdomains in PS-*b*-PEO films owing to its selective distribution to these microdomains.^[39,41,43,45] PDI molecules are suitable for SMT-

SMEP measurements, because the lowest energy electronic transition of the PDI moiety is well-polarized along the long molecular axis. Nile Red and its hydroxylated derivative (NR and NR-OH, respectively; **Figure 2c**) have been used to investigate the local environments of their diffusion pathways in chemically heterogeneous nanostructures on the basis of their solvatochromic properties.^[48,50] These dyes have been incorporated into surfactant micelles, mesoporous silica, and PS-*b*-PEO samples from their precursor solutions, and have been loaded into substrate-supported ONTs by soaking them in dye solutions.

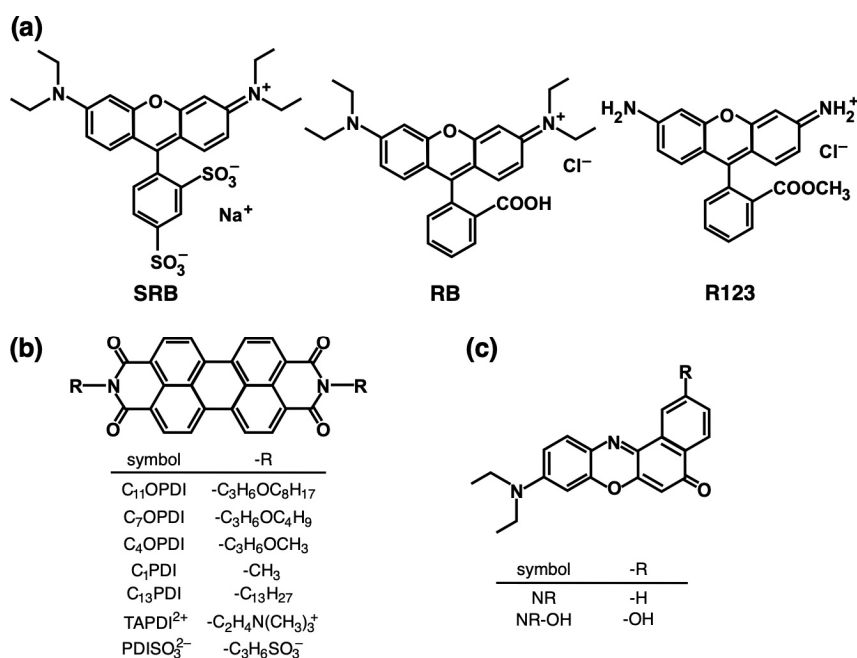


Figure 2. Fluorescent molecules used in our studies.

2.3. SMT and Imaging FCS Measurements

We have recorded SMT and imaging FCS data using a wide-field fluorescence microscope equipped with a laser source, a 100x oil-immersion objective lens of high numerical aperture, and an electron-multiplying charge-coupled device (EM-CCD) (**Figure 3**). Molecular diffusion in the nanostructured materials is slow enough to measure using the EM-CCD at millisecond time resolution. In SMT-SMEP, or in the recording of two-color SMT data, a pair of video images

reflecting different emission polarizations or sample spectral characteristics, can be obtained by placing either a polarizing beamsplitter^[47] or a dichroic beamsplitter and two bandpass filters,^[48] respectively, just before the EM-CCD (**Figure 3**). The position of each dye molecule in each frame of an SMT video has been determined by 2D Gaussian fitting with precision better than the diffraction-limited spatial resolution.^[12] The typical precision, controlled by the signal-to-noise ratios of the fluorescence measurements, was 20-50 nm in our measurements. The locations of a molecule of interest in successive video frames are linked together to obtain a trajectory (**Figure 4, left**).

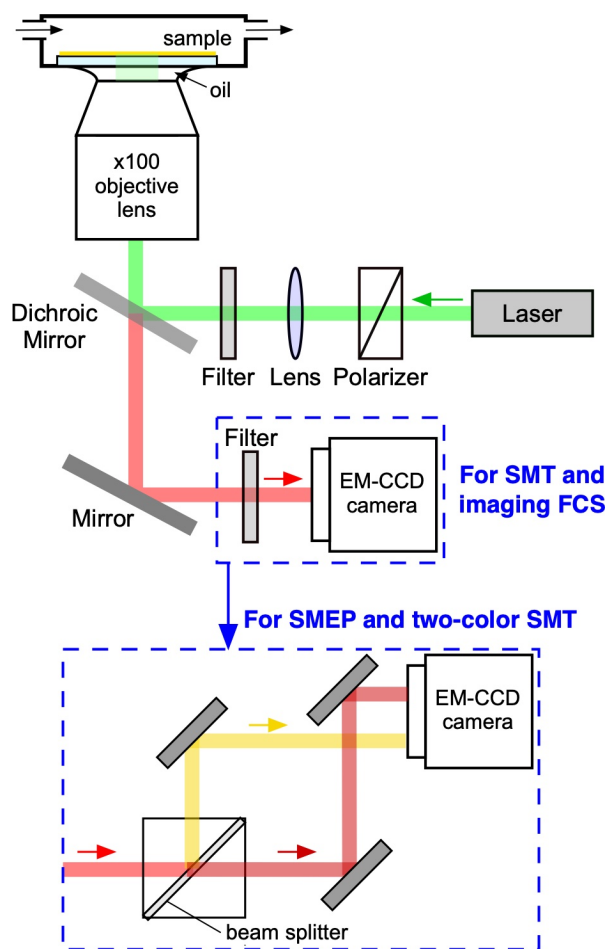


Figure 3. Wide-field fluorescence microscope used in our studies. In SMEP, a polarizing beam splitter is employed. In two-color SMT a beam splitter cube comprising a dichroic beam splitter and appropriate bandpass filters is employed.

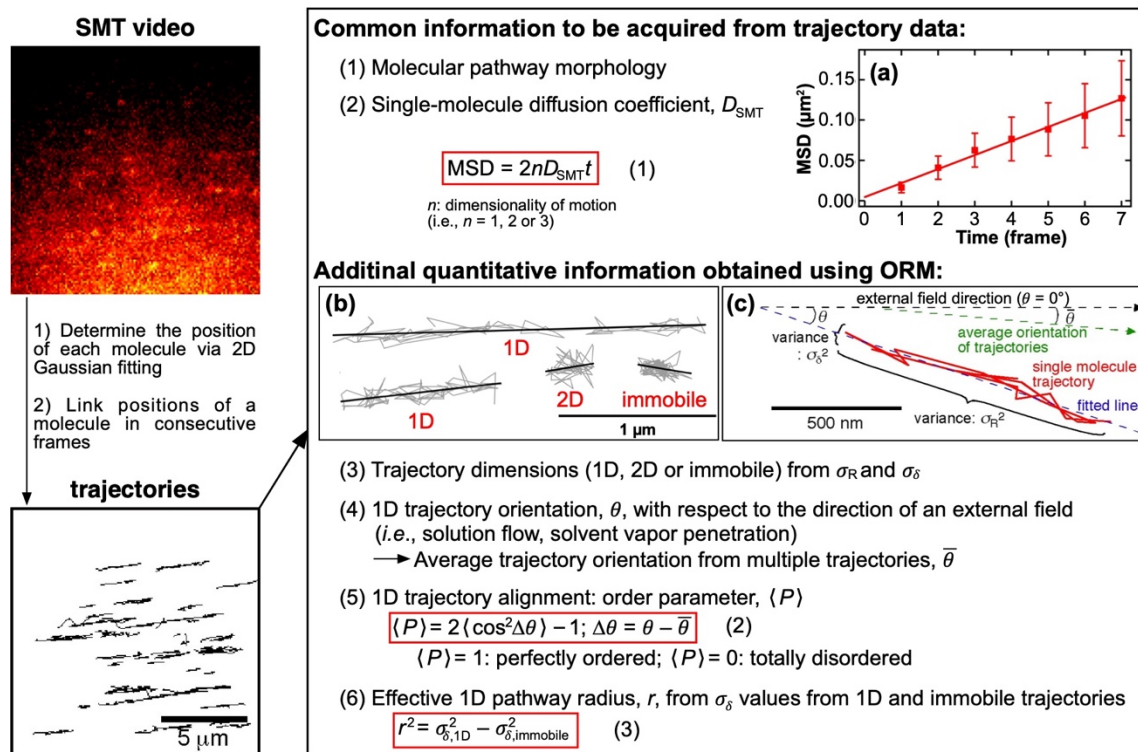


Figure 4. SMT data analysis. **Figure 4a** was depicted from one of trajectories in a SMT video recorded for Ref. 44. The other figures were adapted from Ref. 36 by permission of the PCCP Owner Societies or with permission from Ref. 39. Copyright 2012 American Chemical Society.

2.4. Orthogonal Regression Methods (ORM)

The resulting trajectories provide rich information on the properties of the pathways of individual molecules, and also on their translational dynamics, as summarized in the right box of **Figure 4**. In general, a trajectory can reveal the morphology of a nanostructure that serves to confine and guide molecular motion,^[30,31] as has been confirmed using transmission electron

microscopy.^[30] In addition, the mean square displacement (MSD) of a single molecule may be determined from its trajectory to calculate its diffusion coefficient using Eq (1) (D_{SMT} ; **Figure 4a**).^[57]

The ORM provides a simple means to distinguish 1D trajectories from 2D/immobile ones, and to obtain quantitative information from them. In the ORM, each trajectory is fitted to a line, as shown in **Figure 4b**, and then its longitudinal and transverse variances (σ_{R}^2 and σ_{δ}^2 , respectively; $\sigma_{\text{R}}^2 \geq \sigma_{\delta}^2$) are calculated (**Figure 4c**). 1D trajectories can be separated from 2D/immobile trajectories on the basis of their variance ratio ($= \sigma_{\delta}^2/\sigma_{\text{R}}^2$), which should be smaller than a statistical threshold determined by simulations for 1D motion.^[36] Then, the orientation of each 1D trajectory (θ) can be determined with respect to the direction of an external field applied to align the nanostructures, such as solution flow. The θ values of individual trajectories give their average trajectory orientation ($\bar{\theta}$), permitting an order parameter ($\langle P \rangle$) to be calculated for thin films using Eq (2) in **Figure 4**. The $\langle P \rangle$ value corresponds to the width of the distribution of individual θ , and is consistent to that obtained using ensemble-averaged methods such as X-ray diffraction.^[40] Finally, the effective radius of a 1D molecular pathway (r) can be estimated from the transverse variance of the 1D trajectory ($\sigma_{\delta,1D}^2$) and the average variance of immobile trajectories ($\sigma_{\delta,immobile}^2$) using Eq (3) in **Figure 4**.^[39] Of note, the D_{SMT} , θ , and r values represent the properties of individual molecules/pathways, permitting their distributions to be assessed in much greater detail than can be done using ensemble-averaged data. Meanwhile, the distribution of single-frame step sizes from a 1D trajectory provides insights into material heterogeneity^[44] and/or the exact nature of the mass transport mechanism,^[58,59] which is revealed by fitting the step size distribution to that of a 1D Fickian diffusion model.

2.5. Imaging FCS Measurements and Analysis

We have used imaging FCS^[27] to investigate the diffusion of fluorescent molecules within ONTs under different solution conditions.^[49,51] **Figure 5** summarizes the measurement and analysis procedure. A fluorescence video image (**Figure 5a**) is recorded using a wide-field microscope to obtain fluorescence time transient data at individual pixels (**Figure 5b**). The time transient is then autocorrelated in time using Eq (4), and the resulting autocorrelation function, $C(\tau)$, is fitted to a model equation (**Figure 5c**). Our model equation, Eq (5), has two components associated with 1D Fickian diffusion and photobleaching, and gives the autocorrelation amplitude (A) and the local diffusion coefficient (D_{local}) of dyes at each pixel. The former can be related to the average number of molecules detected at the pixel.^[60] The A and D_{local} values at each position can be plotted to get a spatial distribution of these parameters, as shown in **Figure 5d**. Meanwhile, the permeability of each ONT (D_{ONT}) can be assessed by averaging D_{local} values on the ONT. ONTs in a batch exhibited similar D_{ONT} regardless of their lengths (1 – 9 μm), verifying the homogeneity of their solute releasing properties.^[35,51] The D_{ONT} values for individual ONTs can be further compiled to obtain ensemble-averaged diffusion coefficients (D_{FCS}).

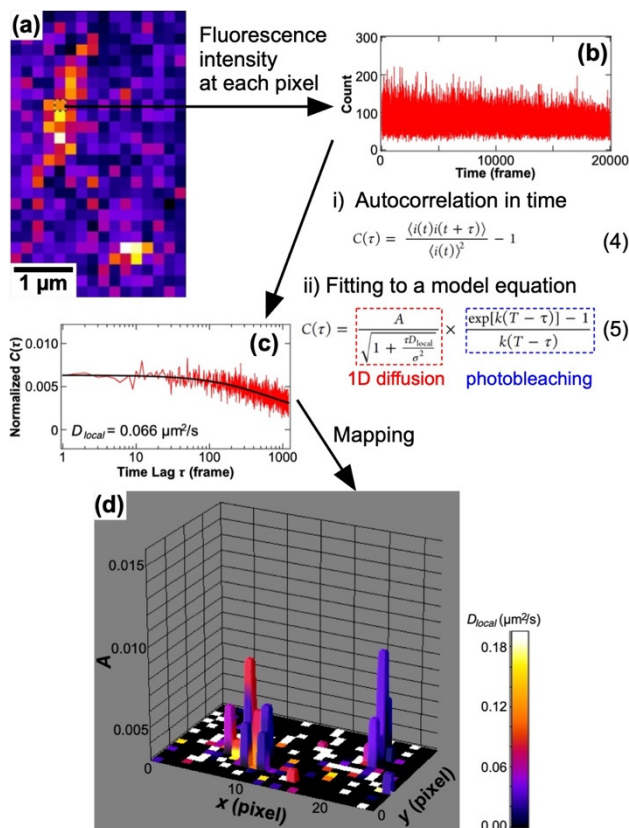


Figure 5. Imaging FCS measurements and data analysis for assessment of molecular diffusion in an ONT. In the measurements, the pixel size was 187.5 nm. Adapted with permission from Ref. 51. Copyright 2019 American Chemical Society.

3. Characterization of Self-Assembled Nanostructures

We have employed SMT to characterize the structural properties (*i.e.*, orientation, order, and radius) of cylindrical nanostructures based on surfactant micelles and BCP microdomains. Our results have shown that SMT can be used to optimize experimental conditions for the fabrication of aligned cylindrical nanostructures, which will be important for their future applications.^[13-15,61]

3.1. Highly-Ordered, Surfactant-Templated Silica Mesopores in Spin-Cast Thin Films

We measured SMT data for C_{11} OPDI molecules diffusing in spin-cast mesoporous silica films templated by rod-shaped CTAB micelles (3.7 nm in diameter from X-ray diffraction).^[34,36]

A number of dye molecules exhibited 1D diffusion, as depicted by the 1D trajectories in **Figure 6a**. Interestingly, ORM analysis of the data revealed the presence of three μm -scale grains consisting of highly-ordered trajectories ($\langle P \rangle \approx 0.9$) but different average trajectory orientations, which was supported by a histogram exhibiting three θ distributions (**Figure 6b**). The observation of these 1D trajectories implied the presence of highly-ordered silica mesopores in each grain. These grains were probably formed via the solvent evaporation-induced self-assembly of template micelles during spin coating.^[62,63]

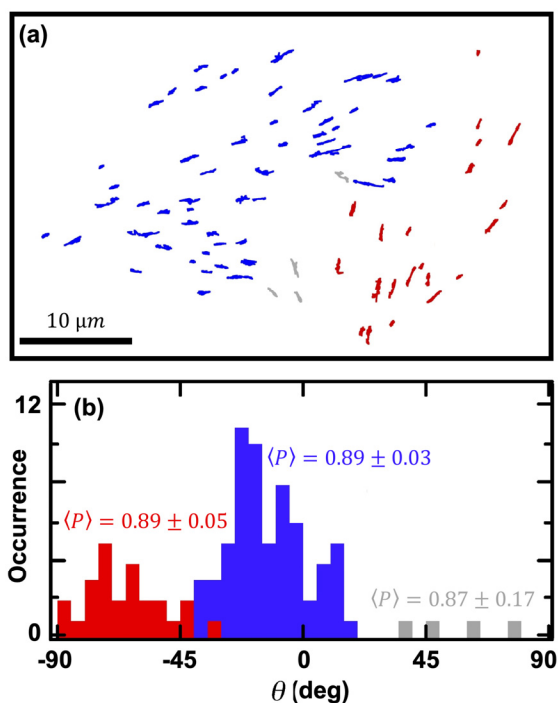


Figure 6. (a) 1D trajectories and (b) their angle histogram from SMT data recorded for C_{11}OPDI molecules diffusing in a spin-cast, CTAB-filled mesoporous silica film under a humidified atmosphere. Adapted from Ref. 36 by permission of the PCCP Owner Societies.

3.2. Flow-Aligned Rod-Shaped Micelles in Microchannel-Incorporated Gels

We sought to align cylindrical surfactant mesophases in the absence^[38] and presence^[40,42] of a silica precursor (tetramethoxysilane, TMOS) by flowing a surfactant gel through a microchannel. We used SMT to assess the orientation of the cylindrical hydrophobic mesophases incorporating

PDI molecules ($C_{11}OPDI$ or $C_{13}PDI$). SMT data showed diffusional motions of these dyes in the longitudinal direction of the microchannel, suggesting the surfactant mesophases could be aligned by shear flow. ORM analysis of the resulting 1D trajectories, however, revealed the lower order of the CTAB mesophases ($\langle P \rangle = 0.6 - 0.85$)^[40] as compared with those in the μm -scale grains of the spin-cast films ($\langle P \rangle \approx 0.9$; **Figure 6**), possibly reflecting the presence of microscopic defects in the mesophases. The shear flow method was also applicable to elongate and align double-stranded DNA molecules incorporated into hexagonal Pluronic F127 mesophases.^[52] On the other hand, an aged TMOS-containing gel afforded poorly-ordered CTAB mesophases owing to the formation of a rigid gel structure as a result of the crosslinking of the silica precursor.^[40]

3.3. Cylindrical BCP Microdomains Aligned by Solvent Vapor Penetration and Shear Flow

We also used SMT to investigate the effects of solvent vapor penetration and shear flow on the elongation and orientation of cylindrical PEO microdomains.^[39,41] The degree of microdomain alignment was quantitatively assessed using the ORM from the diffusional motions of single SRB molecules in a thin PS-*b*-PEO film sandwiched between a glass slide and coverslip (**Figure 7**).

We first sought to align the PEO microdomains by letting solvent vapor penetrate through a PS-*b*-PEO film in the radial direction from the center opening to the outer periphery (**Figure 7a**).^[39] SMT data of 1,4-dioxane-treated films exhibited a large number of 1D-diffusing SRB molecules in the solvent penetration direction (**Figure 7b**) in contrast to those of benzene- or toluene-treated films, indicating that the penetration of 1,4-dioxane vapor induced elongation and alignment of the PEO microdomains. Interestingly, this simple approach was very effective to align microdomains, as shown by very high order parameters ($\langle P \rangle \approx 0.9$) obtained across millimeter distance throughout the entire thickness of the film.

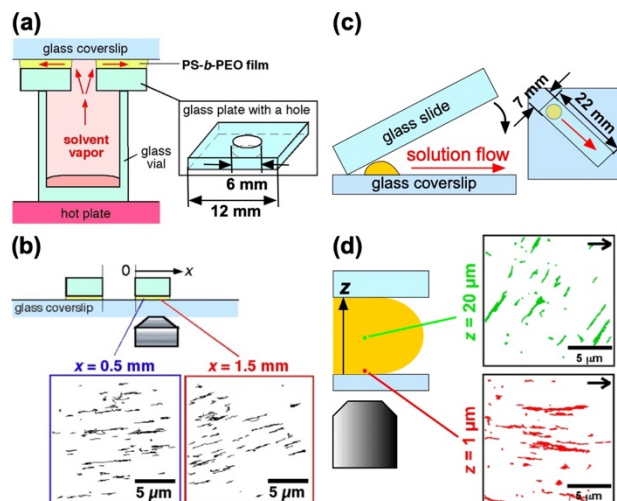


Figure 7. (a) Experimental setup for solvent vapor penetration and (b) trajectories obtained in a PS-*b*-PEO film treated by 1,4-dioxane vapor at two different positions. (c) Procedure of the flow-induced approach and (d) trajectories obtained in a sandwiched PS-*b*-PEO film (arrows: flow direction). Adapted with permission from Refs. 39 and 41. Copyright 2012 and 2014 American Chemical Society.

We also examined the shear flow of a precursor PS-*b*-PEO solution to align cylindrical PEO microdomains.^[41] A droplet of a benzene solution of PS-*b*-PEO (*ca.* 30 wt%) on a coverslip was overlaid with a rectangular glass plate to let the solution flow along the plate, followed by solvent evaporation under N₂ to obtain a sandwiched PS-*b*-PEO film (**Figure 7c**). SMT data revealed that 1D-diffusing molecules in the flow direction were observed at a higher flow rate only near the underlying coverslip ($z = 1 \mu\text{m}$ in **Figure 7d**), implying the alignment of the cylindrical PEO microdomains by shear flow. The SMT data also clarified the presence of μm -scale grains consisting of highly-ordered microdomains with coherent orientation ($\langle P \rangle \approx 0.9$).

The ORM permits us not only to assess the elongation, orientation, and order of cylindrical nanostructures, but also to estimate the effective radius of a nanostructure, as shown in **Figure 4**. Indeed, we estimated the radii of individual microdomains from $\sigma_{\delta,1D}^2$ and $\sigma_{\delta,immobile}^2$ using Eq

(3),^[39] and revealed their reduction associated with the deswelling of the microdomains by solvent evaporation.^[43]

4. Investigations of Molecular Dynamics in Self-Assembled Nanostructures

We have employed fluorescence microscopic techniques to investigate (1) molecular diffusion within surfactant-filled silica mesopores and PEO microdomains, (2) more detailed, orientational dynamics of single molecules and their distributions in surfactant-filled silica mesopores, and (3) the effects of solution conditions on molecular diffusion within individual ONTs.

4.1. Ensemble and Single-Molecule Translational Diffusion Dynamics

We have used SMT to quantify diffusion coefficients of single molecules (D_{SMT}) to gain insights into factors that control translational molecular dynamics in nanostructures. We have also measured molecular diffusion in identical samples using SMT, FCS, and FRAP to assess consistency and difference in information obtained using the single-molecule (SMT) and ensemble-averaged (FCS and FRAP) methods.

4.1.1. Single-Molecule Diffusion Coefficients Measured in Cylindrical Nanostructures

The D_{SMT} values of 1D-diffusing PDI molecules in CTAB-filled mesoporous silica films were three orders of magnitude smaller than the diffusion coefficients of the dyes in bulk solution.^[36,44,46-48] Other researchers also reported similarly slow diffusion of different dye molecules in mesoporous silica films based on other surfactants.^[30,32,33,64] The slow diffusion in these mesoporous silica films could be attributed to the high viscosity of the nanoscale molecular

pathways, and/or to the involvement of desorption-mediated diffusion. Unfortunately, these D_{SMT} values cannot be compared quantitatively, owing to the variation of experimental conditions, especially the uses of different solvent vapors such as water-ethanol^[36,44,46-48] and chloroform^[30,64] for mobilizing dye molecules in these films. Qualitatively, molecular diffusion was enhanced in the presence of solvent at a higher concentration. For example, the D_{SMT} values of C₁₁OPDI diffusing within CTAB-filled silica mesopores were ~100-fold larger in a microfluidics-incorporated monolith^[40] than in spin-cast thin films.^[36] The larger D_{SMT} was attributed to the higher solvent concentration in the former CTAB micelles, as indicated by the more significant swelling of the micelles that was shown by the larger spacing (*ca.* 5.3 nm) of the former^[40] than that of the latter (*ca.* 3.7 nm).^[36] The larger D_{SMT} by solvent-induced swelling was also shown for SRB molecules diffusing within the cylindrical PEO microdomains in PS-*b*-PEO thin films.^[43] Solvent evaporation from flow-aligned thin films (**Figure 7c**) led to gradual decreases in D_{SMT} and effective microdomain radius. Interestingly, these decreases were more significant for PS-*b*-PEO films prepared from THF compared to those from benzene, probably reflecting the better swelling of the PEO microdomains by THF. In addition, a decrease in D_{SMT} was more prominent than that in radius, suggesting the permeability was more susceptible to the presence of solvent.

4.1.2. Direct Comparison between Single-Molecule and Ensemble Diffusion Measurements

Molecular diffusion was measured in identical samples using SMT, FCS, and FRAP to directly compare information obtained using the single-molecule and ensemble-averaged methods. SMT can visualize detailed motions of single molecules at the millisecond timescale, whereas FCS can provide parameters reflecting much quicker motions of a small number of molecules. Thus, these two methods provide complementary information. For example, we measured diffusion data

by SMT and FCS for C₁₃PDI molecules in flow-aligned lyotropic Pluronic F127 mesophases.^[38] FCS exhibited the presence of slower and faster diffusion modes, which could be assigned to molecules diffusing in the more viscous hydrophobic cores and the less viscous corona regions of the micelles, respectively. SMT revealed that the slower diffusion mode was associated with 1D-diffusing molecules in the elongated micelle cores.

Ensemble and single-molecule diffusion behavior of SRB was investigated in identical regions of a 1,4-dioxane-treated PS-*b*-PEO film (**Figure 7a**) using FRAP and SMT.^[45] We first assessed ensemble behavior from diffusion-controlled recovery of fluorescence intensity around a circular photobleached region (**Figure 8a**), followed by SMT measurements in the identical area after the reduction of dye concentration via additional photobleaching (**Figure 8b**). The FRAP data revealed the ensemble-averaged diffusion direction as anisotropic fluorescence recovery in the vapor penetration direction (**Figure 8a**, right), which was consistent with the average of single-molecule diffusion directions from the SMT data (**Figure 8b**, right). The fluorescence recovery speed from the FRAP data provided the ensemble diffusion coefficient of SRB in the PEO microdomains, which was close to the average of D_{SMT} values obtained from SMT data in the identical area. The similarity of the ensemble and single-molecule diffusion data implied the homogeneous structural and chemical properties of the cylindrical PEO microdomains within the measured region. On the other hand, the FRAP data uniquely provided information on long-range microdomain connectivity ($> 100 \mu\text{m}$) from the extent of maximum fluorescence recovery (*ca.* 90%). SMT could be used to assess the distribution of the diffusion direction and D_{SMT} at different distances from the underlying coverslip. These comparisons have revealed that FRAP is suitable to assess ensemble-averaged and longer-range diffusion behavior, whereas SMT can afford more detailed information on molecular dynamics.

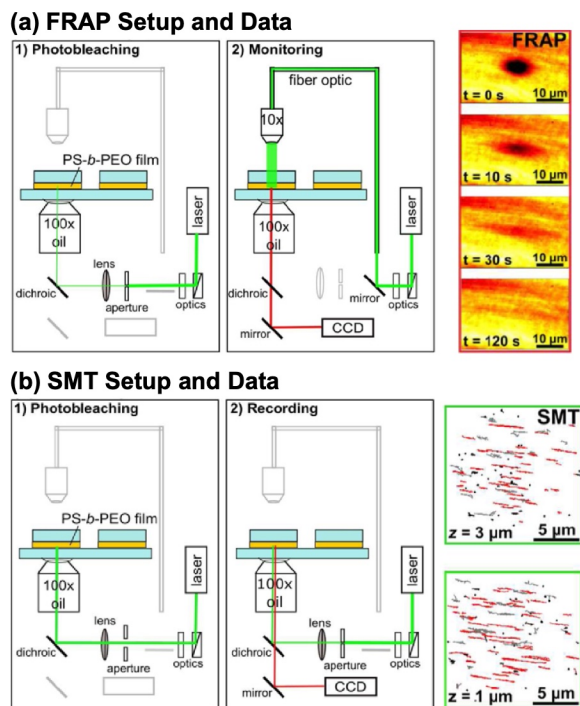


Figure 8. Experimental setups (left) and typical data (right) for (a) FRAP and (b) SMT measurements obtained at a sandwiched PS-*b*-PEO film upon the penetration of 1,4-dioxane vapor (see **Figure 7a**). (a) In FRAP, a circular region (*ca.* 7 μm in diameter) in a PS-*b*-PEO film was photobleached using an intense laser pulse, followed by fluorescence imaging by irradiation with attenuated laser light from the top. (b) Subsequently, SMT data were recorded under broad laser illumination after the wider observation area was further photobleached by more intense laser light. Adapted with permission from Refs. 45. Copyright 2015 American Chemical Society.

4.2. Orientational Dynamics and Distributions of Single Molecules in Self-Assembled Nanostructures

In addition to the translational dynamics, we have also investigated the orientational dynamics and distribution of single PDI and NR molecules diffusing in mesoporous silica thin films.

4.2.1. Orientational Dynamics – Single-Molecule Wobbling

The orientational dynamics of a single molecule can be measured by monitoring its emission polarization after excitation by circularly-polarized light.^[65] We have established a SMT-SMEP method to assess the confined orientational motion (wobbling) of single PDI molecules diffusing in CTAB-filled silica mesopores (**Figure 9a**).^[12,34] In this method, a pair of fluorescence videos are simultaneously recorded in orthogonal polarizations using the microscope shown in **Figure 3**. Polarized emission was observed from PDI molecules (1.4 ~ 2.8 nm long) that were sterically confined along the axis of ≈ 3.7 nm diameter CTAB-filled silica mesopores in spin-cast thin films.^[36,44,46,47,64] In contrast, polarized emission could not be seen even for the longest C₁₁OPDI molecules diffusing in larger pores (≈ 5.3 nm in diameter) filled with solvent-swollen CTAB micelles owing to rapid molecular tumbling.^[40]

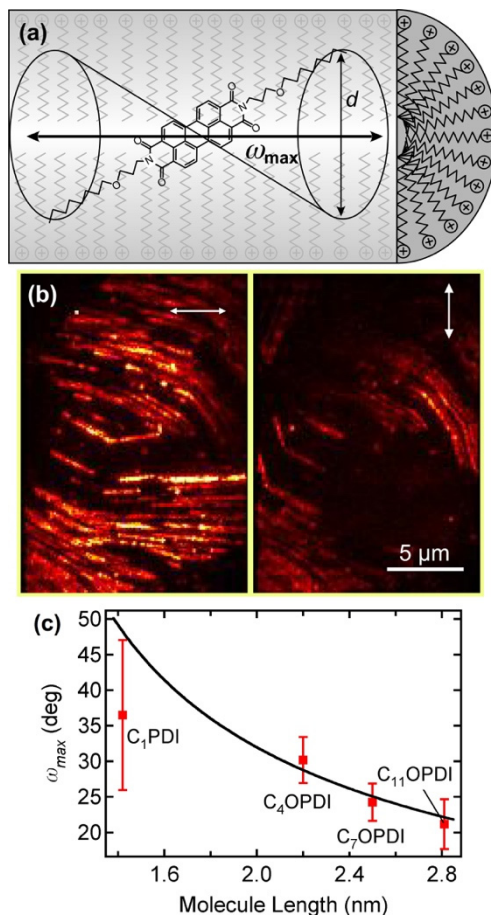


Figure 9. (a) Schematic illustration of a PDI molecule confined to a surfactant-filled silica mesopore. (b) SMEP data exhibiting 1D-diffusing C₇OPDI molecules in a spin-cast, CTAB-templated mesoporous silica film. The images depict the maximum signal level observed at each pixel across the video. Double-ended arrows designate the detected polarizations. (c) Relationship between ω_{\max} and the length of PDI molecules in CTAB-templated mesoporous silica films. Adapted with permission from Ref. 34. Copyright 2013 American Chemical Society.

Figure 9b shows representative SMEP data for C₇OPDI diffusing in the CTAB-filled silica mesopores.^[46] The emission polarization in these experiments was closely aligned with the direction of 1D diffusion for each molecule, indicating that single 1D-diffusing molecules were confined to the pores with their long axes parallel to the long axis of the pore. The emission polarization was quantified by FP , which was obtained from the emission signals of each molecule, I_V and I_H , in the right and left images:^[12,47]

$$FP = \frac{I_V - I_H}{I_V + I_H} \quad (6)$$

Importantly, we found a subtle depolarization in the fluorescence emission, which was attributed to the orientational wobbling of the long axis of the molecule. The time-averaged wobbling angle (ω) of a molecule was calculated from its average orientation, which was assumed to be the same as the trajectory orientation (θ) in the film plane:

$$\langle \cos^2 \omega \rangle = \frac{\cos(2\theta) + FP(2a^2 + 1)}{3\cos(2\theta) + FP(2a^2 - 1)} \quad (7)$$

where a^2 is a constant defining the depolarization by the objective lens. The maximum extent of wobbling, ω_{\max} , could be related to $\langle \cos^2 \omega \rangle$ by:

$$\langle \cos^2 \omega \rangle = \frac{1}{3} \left(\frac{1 - \cos^3 \omega_{\max}}{1 - \cos \omega_{\max}} \right) \quad (8)$$

The ω_{\max} values of the longer PDI molecules were smaller (**Figure 9c**) than those of the shorter molecules, reflecting the effects of steric confinement. Interestingly, the ω_{\max} data from the four PDI dyes permitted the estimation of the transverse diameter of the confinement (~ 1.0 nm), which

was significantly smaller than the silica mesopore diameter (~ 3.7 nm). We attributed this unexpected level of dye confinement to the distribution of the hydrophobic dyes into the CTAB micelle core. Indeed, these four PDI molecules exhibited similarly small D_{SMT} ($0.05 - 0.2 \mu\text{m}^2/\text{s}$), suggesting their presence in similar nanoconfined environments.

4.2.2. Molecular Distributions in Self-Organized Nanostructures

Surfactant-filled mesoporous silica materials comprise hydrophobic micelle cores, hydrophilic micelle coronas, and rigid silica pore walls. The dynamics of fluorescent molecules in these materials are thus controlled by their distribution between these regions, which in turn depends on their hydrophobicity and net charges. We have employed SMT to investigate the diffusion of single molecules and their distribution between different pore environments for differently charged PDI molecules within Pluronic F127-filled silica mesopores in microchannel-incorporated monoliths,^[42] and within CTAB-filled silica mesopores in spin-cast thin films.^[44] In the former study,^[42] the distributions of charged and uncharged PDI dyes within the pores were postulated from their 1D/2D trajectory ratios. An uncharged dye (C_{11}OPDI) exhibited a higher percentage of 1D trajectories, and thus was considered to diffuse in the cylindrical hydrophobic micelle cores. In contrast, charged dyes (TAPDI^{2+} and PDISO_3^{2-}) predominantly gave 2D trajectories, suggesting that these molecules were present in more hydrophilic regions near the pore walls, and could pass through defects in the silica pore wall. In the latter study,^[44] the distributions of PDI molecules were assessed from their translational and orientational dynamics measured using SMT-SMEP. Charged dyes (TAPDI^{2+} and PDISO_3^{2-}) afforded smaller D_{SMT} and larger ω_{max} than uncharged dyes (C_4OPDI and C_{11}OPDI), suggesting their distribution near charged sites at the silica/surfactant boundaries due to electrostatic interactions.

Furthermore, we used two-color SMT and SMT-SMEP to verify the distribution and diffusion behavior of hydrophobic, solvatochromic NR molecules in CTAB-filled silica mesopores.^[48] An E value, which could be related to the dielectric constant (ϵ) of the medium surrounding a single NR molecule, was calculated from the fluorescence intensities of the molecule in two different spectral bands, I_{580} and I_{625} at 580 ± 20 nm and 625 ± 20 nm, using Eq (9):^[66]

$$E \equiv \frac{I_{625} - I_{580}}{I_{625} + I_{580}} = K \left(\frac{\epsilon - 1}{2\epsilon + 1} \right) + C \quad (9)$$

In this equation, K and C were determined by calibration using standard solutions of known ϵ , such as mixtures of *n*-hexane and ethanol. **Figure 10a** shows SMT data simultaneously recorded in the two spectral bands. The E values obtained from individual 1D-trajectories were close to that of *n*-hexane ($E \sim -0.3$), indicating the majority of the NR molecules were located in nonpolar environments. Meanwhile, SMT-SMEP measurements revealed that the fluorescence from 1D-diffusing NR molecules was strongly polarized along the diffusion direction, consistent with orientational motions that were strongly confined to their diffusion pathways. Interestingly, the apparent pathway diameter of the NR molecules was estimated from their wobbling angles to be *ca.* 1 nm, as with PDI molecules. Taken together with the small D_{SMT} values ($\approx 0.08 \mu\text{m}^2/\text{s}$), these results verify that the hydrophobic PDI and NR molecules diffused in the relatively narrow central portions of the nonpolar micelle cores.

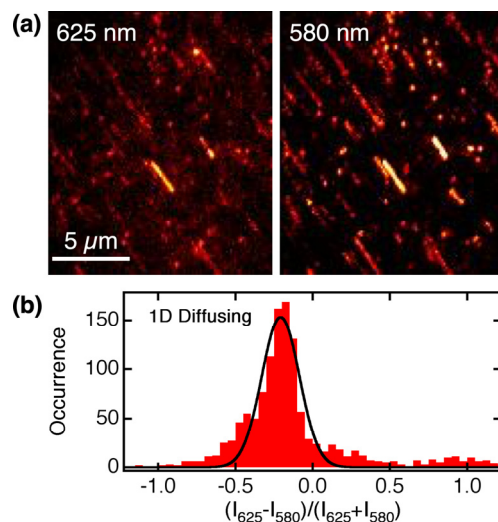


Figure 10. (a) SMT images of single NR molecules recorded in two spectral bands. (b) Distribution of E for 1D-diffusing NR molecules. Adapted with permission from Ref. 48. Copyright 2016 American Chemical Society.

4.3. Molecular Diffusion in Single ONTs

We investigated the diffusion of three differently-charged rhodamine dyes (**Figure 2a**) in individual ONTs (**Figure 1c**) filled with different aqueous solutions using imaging FCS (see **Section 2.5**). **Figure 11a-c** shows the effects of solution pH on the D_{FCS} of anionic SRB, cationic/uncharged-zwitterionic RB, and cationic R123 in single-wall $\text{NH}_2\text{-ONT}_{10\text{nm}}$, single-wall $\text{COOH-ONT}_{10\text{nm}}$, and quadruple-wall $\text{COOH-ONT}_{20\text{nm}}$.^[35,51] Basically, the diffusion of these molecules was controlled by electrostatic interactions that were manipulated by the protonation/deprotonation of the inner $-\text{NH}_2$ and $-\text{COOH}$ groups, as revealed by the pH dependent changes in D_{FCS} . However, relatively hydrophobic RB and R123 in the COOH-ONTs exhibited weak pH-dependent changes in D_{FCS} (**Figure 11bc**), suggesting the involvement of non-Coulombic interactions. The significantly smaller D_{FCS} ($0.01 \sim 0.1 \mu\text{m}^2/\text{s}$) than in aqueous solutions (*ca.* $400 \mu\text{m}^2/\text{s}$) could be attributed to these interactions that induced the adsorption and/or partitioning of the dyes at the interfacial regions of the ONTs on short timescales (**Figure 11d**). Such desorption-mediated diffusion was also suggested from two-color fluorescence

imaging and imaging FCS data obtained for solvatochromic NR and NR-OH (**Figure 2c**) in ethanol-filled NH₂-ONT_{10nm}.^[50] Importantly, pH-dependent changes in D_{FCS} for RB and R123 were less clear in COOH-ONT_{20nm} than in COOH-ONT_{10nm}.^[35] This observation could be attributed to the more significant partitioning of these hydrophobic dyes into the nonpolar walls of quadruple-wall COOH-ONT_{20nm} that were not stabilized by polyglycine-II-type hydrogen bonding networks (**Figure 11e**).

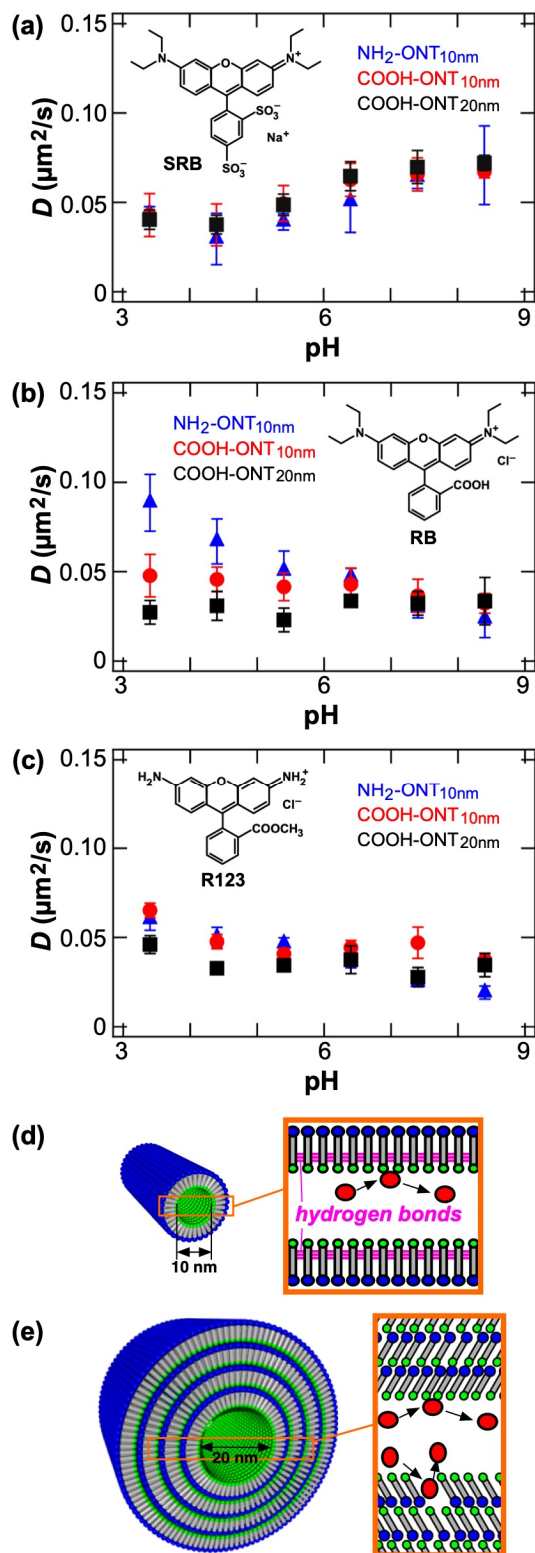


Figure 11. (a-c) D_{FCS} for the three rhodamine dyes as a function of pH (ionic strength: 160 mM). (d,e) Molecular diffusion mechanisms in (d) single-wall and (e) quadruple-wall ONTs. Adapted with permission from Ref. 35. Copyright 2020 American Chemical Society.

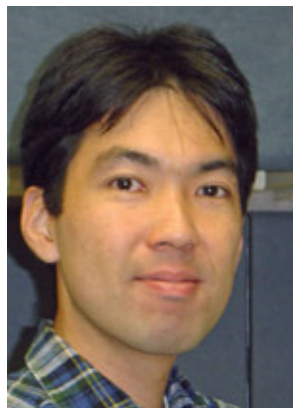
5. Summary and Outlook

In this Personal Account, we have discussed the unique capabilities of fluorescence microscopic techniques in the measurement of detailed molecular dynamics, and also in the characterization of the structural and chemical properties of self-assembled nanostructures. We have established new measurement and analysis methods: The ORM provides the simple means to distinguish between 1D and 2D/immobile trajectories, and to quantify the order, orientation, and effective radii of cylindrical molecular pathways for the optimization of nanostructure preparation. SMT-SMEP permits us to investigate the translational and orientational dynamics of single molecules that revealed the unexpectedly strong nanoconfinement of molecules diffusing in surfactant-filled silica mesopores. Two-color SMT could verify the diffusion pathways of single molecules in surfactant-filled silica mesopores. In addition, we directly compared single-molecule and ensemble-averaged diffusion behaviors to reveal their complementarity as analytical methods. Furthermore, our systematic imaging FCS study revealed the role of a desorption-mediated diffusion mechanism in solute transport in nanoporous media. Overall, our studies have clarified the nanoscale structural and chemical heterogeneity of the self-assembled materials, and their impacts on molecular mass transport dynamics.

Fluorescence microscopic methods will continue to be used to investigate detailed molecular-level processes within nanoporous media relevant to chemical separations and sensing. Indeed, SMT and related techniques have unveiled molecular dynamics at solid-liquid interfaces^[67-70] relevant to chromatography, membrane separations, and electrochemical sensing. In particular, 3D single particle/molecule tracking methods, rather than 2D counterparts introduced in this account, are promising for *in situ* visualization of molecular separation mechanisms in real

membranes.^[71,72] Molecular-level details obtained from these studies will lead to in-depth understanding of the impacts of material heterogeneity on molecular separation mechanisms, and thus will help develop highly efficient separation and sensing media.

Biographical Sketches



Takashi Ito is a Professor of Chemistry at Kansas State University (KSU). He received his B.S. (1993), M.S. (1995), and Ph.D. (1998) degrees in Chemistry from the University of Tokyo. He worked as a Research Associate at Tokyo University of Science, and then as a Postdoctoral Research Associate at Texas A&M University before starting his independent career as an Assistant Professor at KSU in 2004. His current research projects aim to understand the effects of nanoconfinement on mass/charge transport and chemical recognition using electrochemical and microscopic techniques. He currently serves as an editorial board member for *The Chemical Record*.

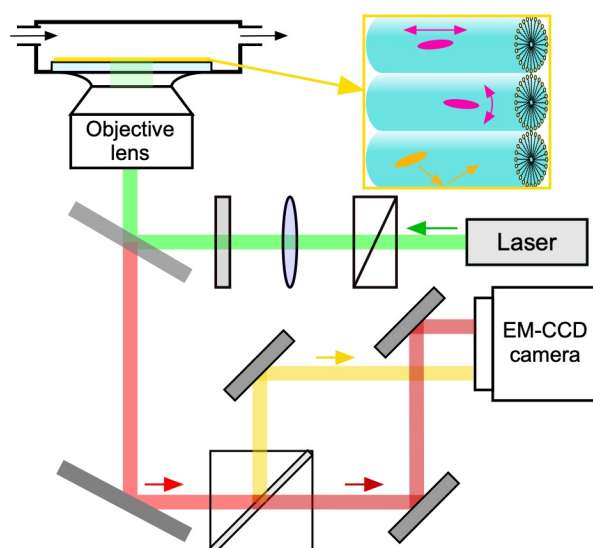


Daniel A. Higgins serves as a Professor and Head of the Chemistry Department at Kansas State University (KSU). He received a B.A. in Chemistry from St. Olaf College in 1988 and a Ph.D. in Chemistry from the University of Wisconsin, Madison in 1993. Afterwards, he did postdoctoral research at the University of Minnesota. He has served on the faculty at KSU since 1996. His group employs optical microscopy and single molecule fluorescence detection and tracking methods to probe the properties of chemical gradients and mesoporous silica materials on nanometer length scales.

Acknowledgements

The authors thank their many co-workers for their contributions to the works described in this personal account. They acknowledge the Division of Chemical Sciences, Geosciences, and Biosciences, Office of Basic Energy Sciences of the U.S. Department of Energy (DE-SC0002362) for financial support of this project.

Graphical Table of Contents



TOC Text

Fluorescence microscopic methods provide unique means to measure detailed molecular dynamics in chemically heterogeneous materials. This paper summarizes our efforts to investigate the molecular-level mechanisms behind molecular permeation in self-assembled cylindrical nanostructures, including surfactant-templated silica mesopores, block copolymer microdomains, and bolaamphiphile-based organic nanotubes. Our studies clarified nanoscale details on the chemical heterogeneity of the nanostructures and their impacts on molecular mass transport dynamics.

References

- [1] S. Terabe, *Annu. Rev. Anal. Chem.* **2009**, *2*, 99–120.
- [2] T. Ikegami, N. Tanaka, *Annu. Rev. Anal. Chem.* **2016**, *9*, 317–342.
- [3] J. R. Werber, C. O. Osuji, M. Elimelech, *Nat. Rev. Mater.* **2016**, *1*, 16018.
- [4] S. P. Nunes, P. Z. Culfaz-Emecen, G. Z. Ramon, T. Visser, G. H. Koops, W. Jin, M. Ulbricht, *J. Membr. Sci.* **2020**, *598*, 117761.
- [5] A. Walcarius, M. M. Collinson, *Annu. Rev. Anal. Chem.* **2009**, *2*, 121–143.
- [6] T. Ito, G. Ghimire, *ChemElectroChem* **2018**, *5*, 2937–2953.
- [7] Z. Ji, H. Wang, S. Canossa, S. Wuttke, O. M. Yaghi, *Adv. Funct. Mater.* **2020**, *30*, 2000238.
- [8] C. M. Doherty, D. Buso, A. J. Hill, S. Furukawa, S. Kitagawa, P. Falcaro, *Acc. Chem. Res.* **2013**, *47*, 396–405.
- [9] B. R. Barnett, M. I. Gonzalez, J. R. Long, *Trends Chem.* **2019**, *1*, 159–171.
- [10] N. S. Bobbitt, M. L. Mendonca, A. J. Howarth, T. Islamoglu, J. T. Hupp, O. L. Farha, R. Q. Snurr, *Chem. Soc. Rev.* **2017**, *46*, 3357–3385.
- [11] M. Hoshino, A. Khutia, H. Xing, Y. Inokuma, M. Fujita, *IUCrJ* **2016**, *3*, 139–151.
- [12] D. A. Higgins, S. C. Park, K.-H. Tran-Ba, T. Ito, *Annu. Rev. Anal. Chem.* **2015**, *8*, 193–216.
- [13] G. Prieto, H. Tuysuz, N. Duyckaerts, J. Knossalla, G.-H. Wang, F. Schuth, *Chem. Rev.* **2016**, *116*, 14056–14119.
- [14] S. L. Suib, *Chem. Rec.* **2017**, *17*, 1–16.
- [15] C. Li, Q. Li, Y. V. Kaneti, D. Hou, Y. Yamauchi, Y. Mai, *Chem. Soc. Rev.* **2020**, *49*, 4681–4736.
- [16] A. J. Bard, L. R. Faulkner, *Electrochemical Methods, Fundamentals and Applications*, 2nd ed., Wiley, New York, **2001**.
- [17] E. L. Cussler, *Diffusion: Mass Transfer in Fluid Systems*, 3rd ed., Cambridge University Press, New York, **2009**.
- [18] L. A. Baker, P. Jin, C. R. Martin, *Crit. Rev. Solid State Mater. Sci.* **2005**, *30*, 183–205.
- [19] A. Yaroshchuk, M. L. Bruening, E. Zholkovskiy, *Adv. Colloid Interface Sci.* **2019**, *268*, 39–63.
- [20] C. S. Johnson, Jr., *Prog. Nucl. Magn. Reson. Spectrosc.* **1999**, *34*, 203–256.
- [21] J. Karger, R. Valiullin, *Chem. Soc. Rev.* **2013**, *42*, 4172–4197.
- [22] H. Jovic, D. N. Theodorou, *Microporous Mesoporous Mater.* **2007**, *102*, 21–50.
- [23] T. Lebold, J. Michaelis, C. Brauchle, *Phys. Chem. Chem. Phys.* **2011**, *13*, 5017–5033.
- [24] H. Coceancigh, D. A. Higgins, T. Ito, *Anal. Chem.* **2019**, *91*, 405–424.
- [25] K. Okamoto, C. J. Shook, L. Bivona, S. B. Lee, D. S. English, *Nano Lett.* **2004**, *4*, 233–239.
- [26] L. Guo, P. Chowdhury, J. Fang, F. Gai, *J. Phys. Chem. B* **2007**, *111*, 14244–14249.
- [27] N. Bag, T. Wohland, M. A. Johnson, T. J. Martinez, *Annu. Rev. Phys. Chem.* **2014**, *65*, 225–248.
- [28] F. Kulzer, T. Xia, M. Orrit, *Angew. Chem. Int. Ed.* **2010**, *49*, 854–866.
- [29] W. E. Moerner, Y. Shechtman, Q. Wang, *Faraday Discuss.* **2015**, *184*, 9–36.
- [30] A. Zurner, J. Kirstein, M. Dobliger, C. Brauchle, T. Bein, *Nature* **2007**, *450*, 705–708.
- [31] M. Yorulmaz, A. Kiraz, A. L. Demirel, *J. Phys. Chem. B* **2009**, *113*, 9640–9643.

- [32] J. Kirstein, B. Platschek, C. Jung, R. Brown, T. Bein, C. Brauchle, *Nat. Mater.* **2007**, *6*, 303–310.
- [33] S. Ito, S. Fukuya, T. Kusumi, Y. Ishibashi, H. Miyasaka, Y. Goto, M. Ikai, T. Tani, S. Inagaki, *J. Phys. Chem. C* **2009**, *113*, 11884–11891.
- [34] D. A. Higgins, K.-H. Tran-Ba, T. Ito, *J. Phys. Chem. Lett.* **2013**, *4*, 3095–3103.
- [35] G. Ghimire, M. M. Moore, R. Leuschen, S. Nagasaka, N. Kameta, M. Masuda, D. A. Higgins, T. Ito, *Langmuir* **2020**, *36*, 6145–6153.
- [36] K. H. Tran Ba, T. A. Everett, T. Ito, D. A. Higgins, *Phys. Chem. Chem. Phys.* **2011**, *13*, 1827–1835.
- [37] K. C. Robben, K.-H. Tran-Ba, T. Ito, D. A. Higgins, *Anal. Chem.* **2014**, *86*, 10820–10827.
- [38] A. W. Kirkemide, T. Torres, T. Ito, D. A. Higgins, *J. Phys. Chem. B* **2011**, *115*, 12736–12743.
- [39] K.-H. Tran-Ba, J. J. Finley, D. A. Higgins, T. Ito, *J. Phys. Chem. Lett.* **2012**, *3*, 1968–1973.
- [40] S. C. Park, T. Ito, D. A. Higgins, *J. Phys. Chem. B* **2013**, *117*, 4222–4230.
- [41] K.-H. Tran-Ba, D. A. Higgins, T. Ito, *J. Phys. Chem. B* **2014**, *118*, 11406–11415.
- [42] S. C. Park, T. Ito, D. A. Higgins, *J. Phys. Chem. C* **2015**, *119*, 26101–26110.
- [43] D. R. Sapkota, K.-H. Tran-Ba, T. Elwell-Cuddy, D. A. Higgins, T. Ito, *J. Phys. Chem. B* **2016**, *120*, 12177–12183.
- [44] R. Kumarasinghe, T. Ito, D. A. Higgins, *Anal. Chem.* **2020**, *92*, 1416–1423.
- [45] K.-H. Tran-Ba, D. A. Higgins, T. Ito, *Anal. Chem.* **2015**, *87*, 5802–5809.
- [46] R. Pramanik, T. Ito, D. A. Higgins, *J. Phys. Chem. C* **2013**, *117*, 15438–15446.
- [47] R. Pramanik, T. Ito, D. A. Higgins, *J. Phys. Chem. C* **2013**, *117*, 3668–3673.
- [48] R. Kumarasinghe, E. D. Higgins, T. Ito, D. A. Higgins, *J. Phys. Chem. C* **2016**, *120*, 715–723.
- [49] H. Xu, S. Nagasaka, N. Kameta, M. Masuda, T. Ito, D. A. Higgins, *Phys. Chem. Chem. Phys.* **2016**, *18*, 16766–16774.
- [50] H. Xu, S. Nagasaka, N. Kameta, M. Masuda, T. Ito, D. A. Higgins, *Phys. Chem. Chem. Phys.* **2017**, *19*, 20040–20048.
- [51] G. Ghimire, R. Espinoza, H. Xu, S. Nagasaka, N. Kameta, M. Masuda, D. A. Higgins, T. Ito, *Langmuir* **2019**, *35*, 7783–7790.
- [52] H. Xu, C. J. Minter, S. Nagasaka, T. Ito, D. A. Higgins, *J. Phys. Chem. B* **2014**, *118*, 4151–4159.
- [53] D. A. Doshi, A. Gibaud, V. Goletto, M. Lu, H. Gerung, B. Ocko, S. M. Han, C. J. Brinker, *J. Am. Chem. Soc.* **2003**, *125*, 11646–11655.
- [54] F. S. Bates, G. H. Fredrickson, *Phys. Today* **1999**, *52*, 32–38.
- [55] P. Huang, Y. Guo, R. P. Quirk, J. Ruan, B. Lotz, E. L. Thomas, B. S. Hsiao, C. A. Avila-Orla, I. Sics, S. Z. D. Cheng, *Polymer* **2006**, *47*, 5457–5466.
- [56] T. Shimizu, W. Ding, N. Kameta, *Chem. Rev.* **2020**, *120*, 2347–2407.
- [57] H. Qian, M. P. Sheetz, E. L. Elson, *Biophys. J.* **1991**, *60*, 910–921.
- [58] R. Walder, N. Nelson, D. K. Schwartz, *Phys. Rev. Lett.* **2011**, *107*, 156102.
- [59] D. Giri, K. M. Ashraf, M. M. Collinson, D. A. Higgins, *J. Phys. Chem. C* **2015**, *119*, 9418–9428.
- [60] F. Ye, M. M. Collinson, D. A. Higgins, *Anal. Chem.* **2007**, *79*, 6465–6472.
- [61] E. A. Jackson, M. A. Hillmyer, *ACS Nano* **2010**, *4*, 3548–3553.
- [62] C. J. Brinker, Y. Lu, A. Sellinger, H. Fan, *Adv. Mater.* **1999**, *11*, 579–585.

- [63] C. Jung, P. Schwaderer, M. Dethlefsen, R. Kohn, J. Michaelis, C. Brauchle, *Nat. Nanotechnol.* **2011**, *6*, 86–91.
- [64] C. Jung, J. Kirstein, B. Platschek, T. Bein, M. Budde, I. Frank, K. Mullen, J. Michaelis, C. Brauchle, *J. Am. Chem. Soc.* **2008**, *130*, 1638–1648.
- [65] C. Reznik, C. F. Landes, *Acc. Chem. Res.* **2012**, *45*, 1927–1935.
- [66] D. Giri, C. N. Hanks, M. M. Collinson, D. A. Higgins, *J. Phys. Chem. C* **2014**, *118*, 6423–6432.
- [67] M. J. Wirth, M. A. Legg, *Annu. Rev. Phys. Chem.* **2007**, *58*, 489–510.
- [68] J. Cooper, J. M. Harris, *Anal. Chem.* **2014**, *86*, 11766–11772.
- [69] N. A. Moringo, H. Shen, L. D. C. Bishop, W. Wang, C. F. Landes, *Annu. Rev. Phys. Chem.* **2018**, *69*, 353–375.
- [70] R. Hao, Z. Peng, B. Zhang, *ACS Omega* **2020**, *5*, 89–97.
- [71] Y. Zhong, G. Wang, *Annu. Rev. Anal. Chem.* **2020**, *13*, 381–403.
- [72] H. Wu, D. K. Schwartz, *Acc. Chem. Res.* **2020**, *53*, 2130–2139.